Key Factor Study for Amphiphilic Block Copolymer-Templated Mesoporous SnO₂ Thin Film Synthesis: Influence of Solvent and Catalyst

Shanshan Yin, Ting Tian, Kerstin S. Wienhold, Christian L. Weindl, Renjun Guo, Matthias Schwartzkopf, Stephan V. Roth, and Peter Müller-Buschbaum*

As a crucial material in the field of energy storage, SnO_2 thin films are widely applied in daily life and have been in the focus of scientific research. Compared to the planar counterpart, mesoporous SnO_2 thin films with high specific surface area possess more attractive physical and chemical properties. In the present work, a novel amphiphilic block copolymer-assisted sol–gel chemistry is utilized for the synthesis of porous tin oxide (SnO_2). Two key factors for the sol–gel stock solution preparation, the solvent category and the catalyst content, are systematically varied to tune the thin film morphologies. A calcination process is performed to remove the polymer template at 500 °C in ambient conditions. The surface morphology and the buried inner structure are probed with scanning electron microscope and grazing-incidence small-angle X-ray scattering. Crystallinity is characterized by X-ray diffraction. The multi-dimensional characterization results suggest that cassiterite SnO_2 with spherical, cylindrical, and vesicular pore structures are obtained. The variation of the film morphology is governed by the preferential affinity of the utilized solvent mixture and the hydrogen bond interaction between the employed cycloether and H_2O molecules in the solution.

S. Yin, T. Tian, K. S. Wienhold, C. L. Weindl, R. Guo,
Prof. P. Müller-Buschbaum
Physik-Department
Technische Universität München
Lehrstuhl für Funktionelle Materialien
James-Franck-Str. 1, Garching 85748, Germany
E-mail: muellerb@ph.tum.de
Dr. M. Schwartzkopf, Prof. S. V. Roth
Deutsches Elektronen-Synchrotron DESY
Notkestr. 85, Hamburg 22603, Germany
Prof. S. V. Roth
Department of Fibre and Polymer Technology
KTH Royal Institute of Technology
Teknikringen 56–58, Stockholm SE-100 44, Sweden
Prof. P. Müller-Buschbaum
Heinz Maier-Leibnitz Zentrum (MLZ)
Technische Universität München
Lichtenbergstr. 1, Garching 85748, Germany

The ORCID identification number(s) for the author(s) of this article can be found under https://doi.org/10.1002/admi.202001002.

1. Introduction

Nanostructured SnO_2 thin films were widely investigated during the past decades because of its wide band gap. Accordingly, they are used in various applications such as lithium-ion batteries,[1–11] solar cells,[12–20] solar water splitting,[21] gas sensing [20,22–32] and photoluminescence.[33] Methods reported in the literature for preparing nanostructured SnO_2 thin films include solvothermal synthesis,[3,34,35] reverse microemulsion synthesis,[36] sol–gel synthesis,[37–43] sputter deposition,[28,44] chemical vapor deposition,[29,33,45] electro spinning,[46] and electro deposition.[47] Among these preparation approaches, in particular the block copolymer-assisted sol–gel chemistry approach features advantages in terms of enabling a large-scale production, since most of the sol–gel reaction can be performed without complicated equipment in ambient conditions. Moreover, it is possible to assemble inorganic clusters into thin films with well-controlled crystal sizes, composition, and homogeneity.[48] For example, Brezesinski and co-authors synthesized crack-free, mesoporous SnO_2 films by using the amphiphilic diblock copolymer poly(ethylene-*co*-butylene)-block-poly(ethylene oxide) and the crystallization mechanisms as well as the mesostructural evolution were investigated by a specially constructed 2D small-angle X-ray scattering setup.[49] Roose and co-authors fabricated mesoporous SnO_2 electron selective contacts of perovskite solar cells based on the block copolymer poly(1,4-isoprene-*b*-ethylene oxide) to achieve stable perovskite solar cells, which showed good performance under UV light in an inert atmosphere.[15] Chi and co-authors synthesized a series of mesoporous SnO_2 thin films with the amphiphilic graft copolymer poly(vinyl chloride)-*g*-poly(oxyethylene methacrylate), which showed significantly different gas-sensing performances as a function of the SnO_2 porosity.[30] Although mesoporous SnO_2 thin films prepared with block copolymer templates have shown applications in many fields, the key factors governing the final film morphology during the preparation process were rarely discussed. However, a more detailed understanding of the reaction conditions for the block copolymer-assisted sol–gel chemistry approach to synthesize

**ADVANCED
SCIENCE NEWS**
www.advancedsciencenews.com

**ADVANCED
MATERIALS
INTERFACES**
www.advmatinterfaces.de

mesoporous SnO₂ thin films will be a crucial factor for real-world application.

Typically, the following requirements are supposed to be met during the preparation of metal oxide thin films with block copolymer-assisted sol–gel chemistry. A good solvent for both polymer blocks is required for dissolving the block copolymer and a poor solvent for one of the blocks is required for stimulating the phase separation of the sol–gel system. To avoid the occurrence of macroscopic phase separation in the sol–gel solution, a good miscibility between good and poor solvent is necessary. In order to integrate the functional inorganic part into the micro-phase-separated block polymer network, a hydrogen bond interaction between the precursor molecules and a specific segment of the block copolymer template is expected.[48] According to previous studies, the factors that affect the microstructure of the block copolymer-templated metal oxide thin films include the reaction time,[49] the component content,[50–52] the surface conditions of the substrate,[53] the operational environment,[54] and the way of removing the polymer template.[55]

In the present study, the amphiphilic diblock copolymer polystyrene-block-poly(ethylene oxide) (PS-*b*-PEO) is utilized as template and SnCl₄ is utilized as precursor to fabricate mesoporous SnO₂ thin films. A morphology control of the SnO₂ thin films is realized by changing two key factors in the sol–gel stock solution: the content of hydrochloric acid catalyst and the category of the organic solvent (tetrahydrofuran (THF) or 1,4-dioxane). As a poor solvent to the PS blocks, the preferential affinity of the solvent to the different polymer blocks can be significantly changed with the addition of hydrochloric acid. Through the complexation effect between SnCl₄ and the solvent molecules (THF or 1,4-dioxane), the SnCl₄ precursor can be temporarily frozen-in before adding hydrochloric acid as catalyst. This leads to the sustained release and a controlled hydrolysis of SnCl₄. As a consequence, the formation of big clusters due to the rapid hydrolysis of SnCl₄ is significantly inhibited and a mesoscale structure can be formed. Due to the synergistic effect of hydrochloric acid and the organic solvent, different mesopore structures such as spherical, cylindrical, and vesical structures

are successfully obtained. The thin film morphologies in the local and large area are probed with scanning electron microscopy (SEM) and grazing-incidence small angle X-ray scattering (GISAXS). By correlating different characterization results with the thin film preparation method, the thin film morphology evolution is understood to originate from the preferential affinity of the utilized solvent mixture and the hydrogen bond interaction between the cycloether and H₂O molecules.

2. Result and Discussion

The complexation between SnCl₄ and the solvent molecules (THF or 1,4-dioxane) is schematically shown in **Figure 1**a. The existence of these complexes prevents the intense hydrolysis of SnCl₄ from the addition of hydrochloric acid, which accordingly restricts the aggregation of the hydrolyzed $(HO)_X SnCl_{4-X}$ ($0 \leq x \leq 4$) species in the sol–gel solution. Through hydrogen bond interaction, the $(HO)_X SnCl_{4-X}$ species are specially confined into the hydrophilic PEO domains of the phase separated system (Figure 1b). The common phase-separated structures, such as spheres, cylinders, lamella, and vesicles, can be formed by the PS-*b*-PEO polymer template and the hydrolyzed products in the sol–gel system are demonstrated in Figure 1c.

2.1. Crystallinity of the Calcined Thin Films

For a specific chemical reaction, the equilibrium constant K is a measure of the ratio of the concentrations of products to the concentrations of reactants, which can be calculated by its corresponding standard Gibbs free energy (ΔG^0) with

$$\ln K = -\frac{\Delta G^0}{RT} \tag{1}$$

R is the gas constant with a value of 8.314 J K⁻¹ mol⁻¹, T is the temperature of the reaction, ΔG^0 is the Gibbs free energy
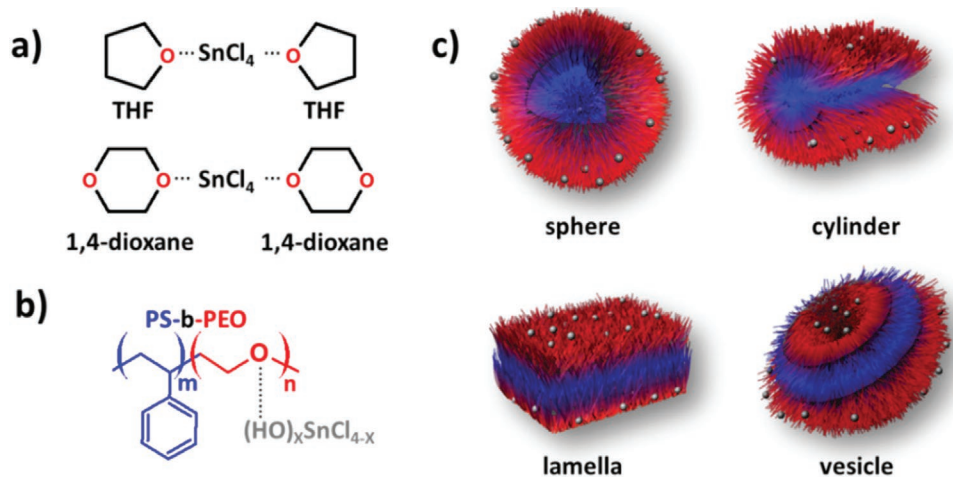

Figure 1. a). Complexation between solvent molecules and SnCl₄ precursor; b) hydrogen-bond interaction between the hydrolyzed product of SnCl₄ and the PEO block; c) common phase-separated structures formed by amphiphilic diblock copolymers, PS blocks, PEO blocks, and hydrolyzed $(HO)_X SnCl_{4-X}$ ($0 \leq x \leq 4$) species are shown in blue, red, and white colors, respectively.

**ADVANCED
SCIENCE NEWS**

www.advancedsciencenews.com

**ADVANCED
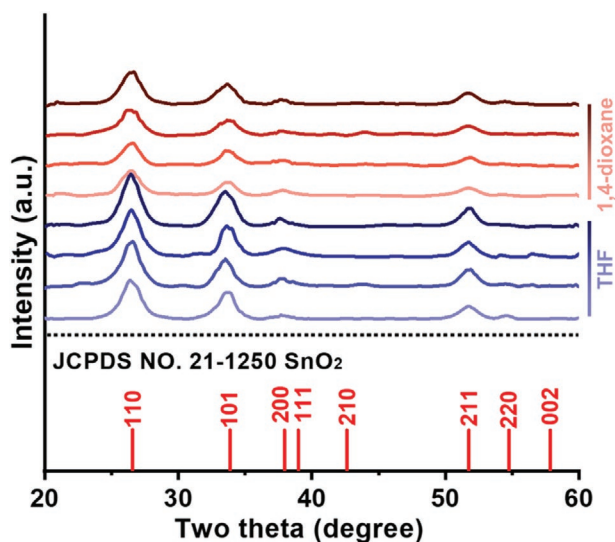MATERIALS
INTERFACES**

www.advmatinterfaces.de

Figure 2. XRD patterns of the calcined SnO_2 thin films. The SnO_2 thin films prepared with THF solvent and 1,4-dioxane solvent are represented as blue and red colors, respectively. The gradually darkening colors are utilized to represent the increment of the hydrochloric acid content.

Table 1. The calculated grain sizes of different SnO_2 thin films prepared with different hydrochloric acid content.

Solvent	Grain sizes of SnO_2 [nm]			
	50 µL	100 µL	150 µL	200 µL
THF	5.1 ± 0.3	5.5 ± 0.2	5.4 ± 0.2	5.2 ± 0.4
1,4-dioxane	5.2 ± 0.4	5.5 ± 0.2	4.8 ± 0.3	4.9 ± 0.3

the experimental result of previous work.[38] In addition, the thin films acquired with THF solvent exhibit higher XRD peak intensities than that of the 1,4-dioxane counterpart. This difference can be assigned to the relatively larger film thickness as indicated in the cross-section SEM images in Figure S2 in the Supporting Information. The different boiling points of the utilized solvents likely account for the thickness difference. Compared with the low boiling point THF system, the slower evaporation rate of the 1,4-dioxane solvent during the spin coating slackened the vitrification process of the thin film. As a consequence, more solution is lost at the same centripetal force level during the spin-coating process, which in turn decreased the film thicknesses. The small grain sizes in the SnO_2 thin films will give rise to unique physical and chemical properties being of great potential in various applications.

2.2. Film Surface Morphology

Figure 3a–d shows the SEM images and corresponding fast Fourier transform (FFT) patterns of the SnO_2 thin films prepared with THF solvent. The hydrochloric acid content added in the sol–gel solution is 50, 100, 150, and 200 µL (Figure 3a–d). All thin films prepared with THF solvent exhibit randomly distributed mesoporous structures. No significant structure variation is demonstrated with progressive hydrochloric acid addition. The weak order of the mesoporous structures can be further revealed by the corresponding blurred ring-like FFT patterns of the SEM images. In comparison with the THF system, the SnO_2 thin films prepared with 1,4-dioxane exhibit more intriguing microstructures, such as cylinders and vesicles. Moreover, the FFT pattern of the thin film prepared with 50 µL hydrochloric acid demonstrates conspicuous hexagonal symmetry patterns (Figure 3e), which suggests the existence of hexagonally ordered mesoporous structures of the thin film. In addition, a porous structure similar to Figure 3a is obtained when the hydrochloric acid amount is increased to 100 µL (Figure 3f). However, the relative blurred FFT patterns suggest the smearing of the hexagonally ordered mesopore arrangement. With further hydrochloric acid addition, a novel hybrid nanostructure consisting of spheres and cylinders is obtained (Figure 3g). The FFT pattern in Figure 3g reveals the random structure arrangement of the thin film. When the hydrochloric acid content utilized for sol–gel solution preparation is increased to 200 µL, a coexisting nanostructure of cylinders and vesicles is obtained (Figure 3h). The cross-section images shown in Figure S2 in the Supporting Information demonstrate that the thickness of all thin films is around 100 nm.

To quantitatively extract contributions from different spatial frequencies, a power spectral density (PSD) function for

change per mole of reaction for unmixed reactants and products at standard conditions (i.e., 298 K, 100 kPa, 1 M of each reactant and product). A study about the temperature dependence of the equilibrium constant K showed that the $\ln K$ value for reaction (2) was positive after the temperature reached 100 °C, which favors the formation of the SnO_2 product at equilibrium[58]

$$SnCl_4\,(l) + 2H_2O(l) \rightarrow SnO_2 + 4HCl(g) \qquad (2)$$
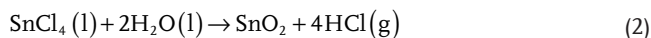
With a custom-built 2D small-angle X-ray scattering setup, Smarsly and co-authors demonstrated the pronounced crystallization of SnO_2 synthesized with poly(ethylene-*co*-butylene)-block-poly(ethylene oxide) template to occur at around 300–350 °C.[49] In order to determine the crystallinity of the calcined SnO_2 thin films prepared in the present work, X-ray diffraction (XRD) measurement is performed (**Figure 2**). The distinct diffraction peaks at 26.6°, 33.9°, 37.9°, 39.0°, 42.6°, 51.7°, 54.7°, and 57.8° are assigned to the (110), (101), (200), (111), (210), (211), (220), and (002) crystal planes of the SnO_2 cassiterite phase (JCPDS NO. 21-1250). The crystal size of the SnO_2 nanostructures can be calculated with the Debye–Scherrer equation

$$D = \frac{0.9\lambda}{\beta\cos\theta} \qquad (3)$$

where λ denotes the wavelength of the X-rays, β and θ refer to the full-width at half-maximum and Bragg angle of the peaks, respectively. The average crystal sizes of the SnO_2 thin films are calculated from the (110), (101), and (211) peaks of the XRD patterns and the corresponding results are listed in **Table 1**. It is observed that the grain sizes of all SnO_2 thin films are around 5 nm and independent of the utilized solvent categories and hydrochloric acid content added into the sol–gel solution. The grain sizes listed in Table 1 are likely determined by the high calcination temperature, which is in accordance with

**ADVANCED
SCIENCE NEWS**
www.advancedsciencenews.com

**ADVANCED
MATERIALS
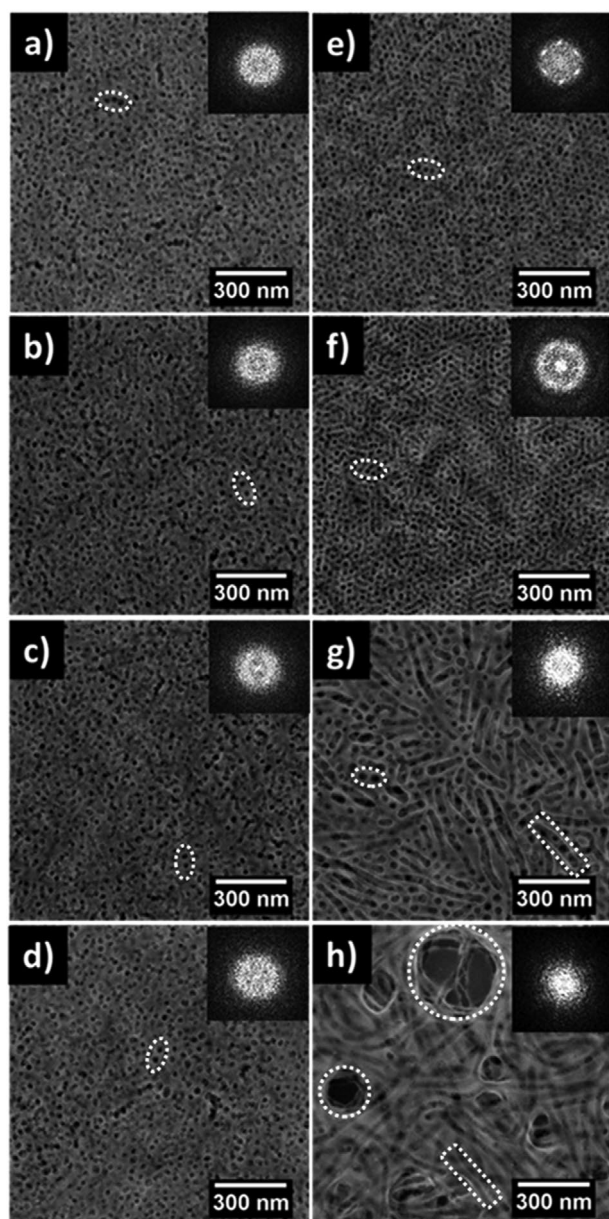INTERFACES**
www.advmatinterfaces.de

Figure 3. SEM images and corresponding FFT patterns (upper right insets) of the samples prepared with a–d) THF and e–h) 1,4-dioxane. The corresponding hydrochloric acid contents added into the sol–gel solution are a,e) 50, b,f) 100, c,g) 150, and d,h) 200 µL. The spherical, cylindrical, and vesicle nanostructures in the SEM images are marked with ellipse, rectangle, and circle, respectively.

tively. For the 1,4-dioxane system, the PSD profiles of the thin films prepared with 50 and 100 µL hydrochloric acid feature a sharp single peak, and the peak positions at 0.2380 and 0.2174 nm^{-1} correspond to an average interdomain spacing of 26 and 29 nm, respectively. In contrast, when the hydrochloric acid addition is further increased to 150 or 200 µL, multiple maxima in the PSD profile distribution are seen, which suggests the existence of polydisperse structures. The most pronounced peak is located at 0.1389 and 0.0799 nm^{-1} for the thin films prepared with 150 and 200 µL hydrochloric acid. It corresponds to a dominant interdomain distance of 45 and 79 nm, respectively. Compared to the PSD profiles of the thin films prepared with THF solvent, a more pronounced variation of the peak width and position is observed for the 1,4-dioxane counterpart, which suggests a significant change of the order and interdomain distances on the film surface.

2.3. Inner Film Morphology

With SEM, the local surface morphologies of the prepared SnO_2 thin films are clearly visualized. However, the porosity for the buried structures is also of great importance for practical applications. Accordingly, GISAXS measurements are performed to probe both the surface and the inner structures of the thin films within a large sample area. Figure S5 in the Supporting Information shows the GISAXS measurement geometry. The horizontally positioned thin film samples are illuminated by an incident X-ray beam with a shallow incident angle (0.4°). The transmitted and reflected beams from the thin film are denoted as direct beam (*D*) and specular beam (*S*), respectively. The maximum scattering intensity between specular beam and direct beam refers to the so-called Yoneda peak, which is given by the maximum in the Fresnel transmission function and depends on the material.[60]

Figure 4a–d refers to the 2D GISAXS data of the SnO_2 thin films prepared with THF solvent and different hydrochloric acid addition content. The specular beam is blocked by a circular beam stop to prevent oversaturation of the detector. As indicated in Figure 4a–d, all of the scattering patterns show a distinct scattering signal in the Yoneda region, and the sectorial scattering patterns indicate the existence of randomly oriented nanostructures inside the entire films.[61] For a quantitative structure analysis in lateral direction, horizontal line cuts are performed for the 2D GISAXS data at the critical angle of SnO_2. The specific position is marked with a red arrow in Figure 4a. The corresponding line cuts are plotted in Figure 4i. All line cuts exhibit multiple intensity peaks, as indicated with the black arrows. The prominent second-order peak position of the thin film prepared with 50 µL hydrochloric acid addition is marked with a black dash line for reference. The gradual left shift of the second-order peak position from bottom to top indicates a progressive expansion of the detected feature size with hydrochloric acid addition. Moreover, the gradual smearing of the peaks in the line cuts with increasing hydrochloric acid addition indicates an enhanced disorder, which is in good agreement with the characteristics of the PSD profiles shown in Figure S3 in the Supporting Information.

each porous SnO_2 thin film is calculated from the SEM data. As shown in Figure S3 in the Supporting Information, distinct PSD profile distributions are observed for the SnO_2 thin films prepared with different solvents and hydrochloric acid addition. Specifically, a clear broad single peak is observed in each PSD profile of the THF system. The peak positions at 0.1921, 0.1806, 0.1770, and 0.1736 nm^{-1} for the thin films prepared with 50, 100, 150, and 200 µL hydrochloric acid addition correspond to an average interdomain spacing of 33, 35, 36, and 36 nm, respec-

**ADVANCED
SCIENCE NEWS**

www.advancedsciencenews.com

**ADVANCED
MATERIALS
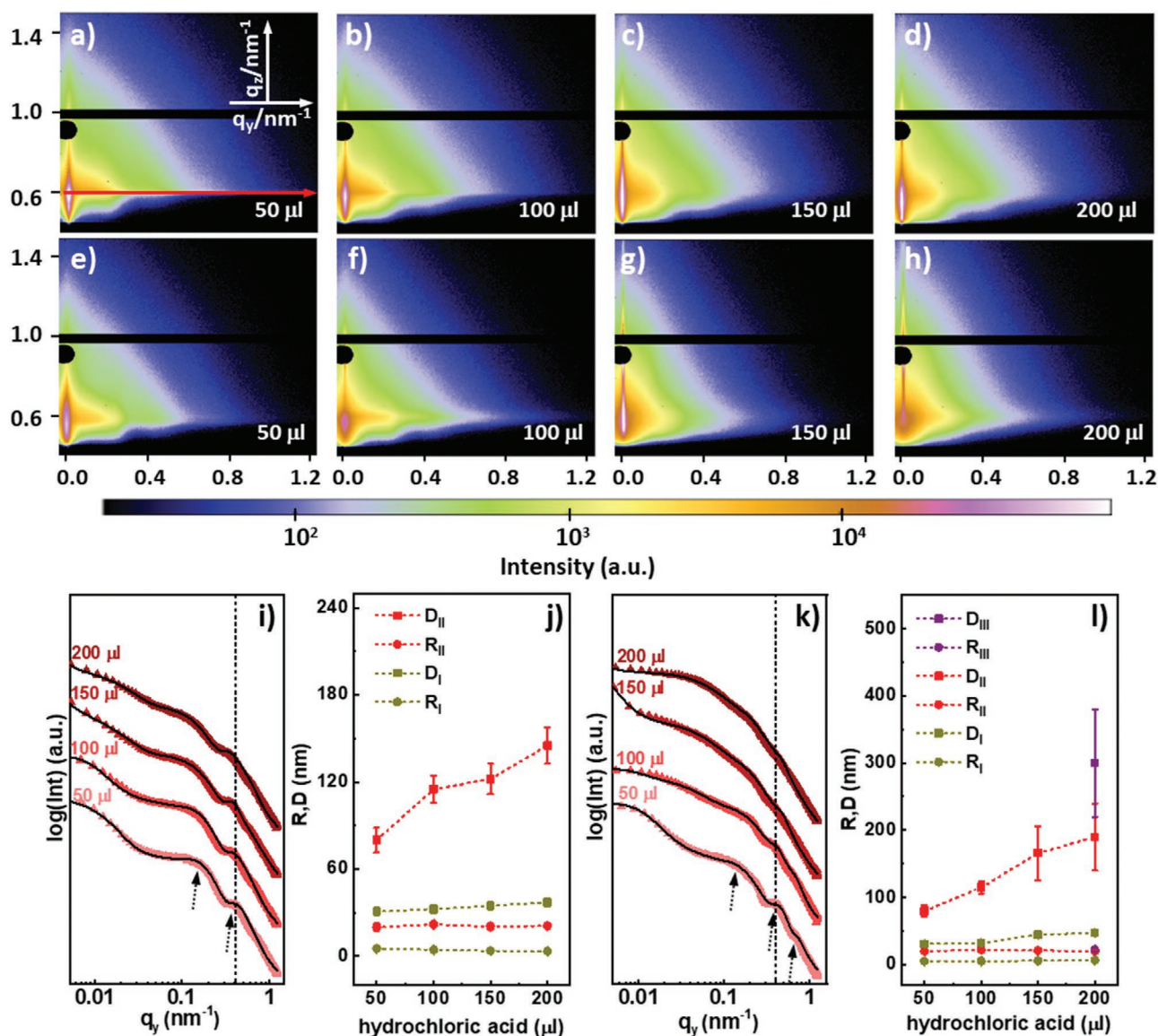INTERFACES**

www.advmatinterfaces.de

Figure 4. 2D GISAXS data of the SnO$_2$ thin films prepared with a–d) THF solvent and e–h) 1,4-dioxane. The hydrochloric acid content utilized for the stock solution preparation is denoted on the lower right corner of each frame. Horizontal line cuts of the thin films prepared with i) THF solvent and k) 1,4-dioxane solvent, respectively. The measured data are plotted as solid triangles and the fit results are shown as black lines, respectively. All curves are shifted along the intensity axis for clarity of the presentation. Extracted structure radii (R) and center-to-center distances (D) given as a function of the hydrochloric acid content are the extracted feature sizes of the thin films prepared with j) THF solvent and l) 1,4-dioxane solvent, respectively. The small-sized, medium-sized, and large-sized structures are represented as dark yellow, red, and purple color, respectively.

Figure 4e–h refers to the 2D GISAXS data of the thin films prepared with 1,4-dioxane solvent. A distinct smearing of the Bragg peak is found with increasing hydrochloric acid addition, which can be more clearly revealed in the horizontal line cuts (Figure 4k). The prominent second-order peak position of the thin film prepared with 50 µL hydrochloric acid addition is marked with a black dash line for reference. Apart from the second-order peak, a distinct third-order peak as marked with the black arrow is observed in the horizontal line cut of the sample prepared with 50 µL hydrochloric acid addition, which suggests the existence of well-ordered structures in the thin film. With further hydrochloric acid

addition, the scattering peaks in the higher q-region are gradually smeared out while an enhanced intensity in the lower q-region occurs simultaneously, which reflects the enhanced disorder of the small structures and increased contribution from large structures.

In order to extract more detailed information of the nanostructures, the horizontal line cuts in Figure 4i,k are modeled within the framework of the distorted-wave Born approximation (DWBA). A 1D paracrystalline lattice and a Gaussian size distribution are assumed for modeling the structure and form factors.[59] The feature sizes including radii and center-to-center distances of the nanostructures are extracted by modeling.

**ADVANCED
SCIENCE NEWS**

www.advancedsciencenews.com

**ADVANCED
MATERIALS
INTERFACES**

www.advmatinterfaces.de

Table 2. Modeled feature sizes in terms of structure radii (R) and center-to-center distances (D) of the thin films prepared with THF solvent.

Hydrochloric acid (µL)	Feature sizes [nm]			
	D_I	R_I	D_{II}	R_{II}
50	31 ± 3	5.2 ± 0.5	80 ± 9	20 ± 3
100	33 ± 3	4.4 ± 0.5	115 ± 9	22 ± 2
150	35 ± 3	3.8 ± 0.4	122 ± 11	21 ± 2
200	37 ± 3	3.4 ± 0.4	145 ± 13	21 ± 2

Based on the modeled radii and center-to-center distance, the pore sizes can be extracted with the following equation[62]

$$Pore\ size = center\text{-}to\text{-}center\ distance - 2 \times structure\ radius \qquad (4)$$

In order to obtain reasonable modeling result, two and three sets of feature sizes are used to model the line cuts in Figure 4i,k, respectively. The specific modeling results for the line cuts in Figure 4i are shown in Figure 4j and **Table 2**. With the progressive hydrochloric acid addition, the radii remain almost constant while the center-to-center distances increase gradually for both small and large structures. For the small structures, the center-to-center distances of the thin films prepared with 50, 100, 150, and 200 µL hydrochloric acid addition are determined to be (31 ± 3), (33 ± 3), (35 ± 3), and (37 ± 3) nm. The corresponding structure radii are (5.2 ± 0.5), (4.4 ± 0.5), (3.8 ± 0.4), and (3.4 ± 0.4) nm, respectively. For the medium-sized structures, the center-to-center distances of the thin films prepared with 50, 100, 150, and 200 µL hydrochloric acid addition are (80 ± 9), (115 ± 9), (122 ± 11), and (145 ± 13) nm. The corresponding structure radii are (20 ± 3), (22 ± 2), (21 ± 2), and (21 ± 2) nm, respectively.

As a result, the small pore sizes of the thin films prepared with 50, 100, 150, and 200 µL hydrochloric acid are (20 ± 4), (24 ± 4), (27 ± 4), and (30 ± 4) nm, respectively. The medium pore sizes of these films are (40 ± 14), (71 ± 13), (81 ± 15), and (103 ± 16) nm.

The specific modeling results for Figure 4k are shown in Figure 4l and **Table 3**. The line cuts of the thin films prepared with 50, 100, and 150 µL hydrochloric acid are fitted with two structure factors and form factors, and the thin film prepared with 200 µL hydrochloric acid is fitted with three structure factors and forms factors, respectively. For the small structures, the center-to-center distances of the thin films prepared with 50, 100, 150, and 200 µL hydrochloric acid are (31 ± 3), (32 ± 3),

Table 3. Modeled feature sizes in terms of structure radii (R) and center-to-center distances (D) of the thin films prepared with 1,4-dioxane solvent.

Hydrochloric acid (µL)	Feature sizes [nm]					
	D_I	R_I	D_{II}	R_{II}	D_{III}	R_{III}
50	31 ± 3	5.4 ± 0.5	80 ± 9	20 ± 3	–	–
100	32 ± 3	5.1 ± 0.5	115 ± 9	22 ± 2	–	–
150	45 ± 3	6.0 ± 0.4	166 ± 40	21 ± 2	–	–
200	47 ± 3	6.5 ± 0.5	190 ± 50	20 ± 2	300 ± 80	22 ± 2

(45 ± 3), and (47 ± 3) nm. The corresponding structure radii are (5.4 ± 0.5), (5.1 ± 0.5), (6.0 ± 0.4), and (6.5 ± 0.5) nm. Using Equation (4), the pore sizes for the small structures are calculated to be (20 ± 4), (22 ± 4), (33 ± 3), and (34 ± 4) nm. For the medium-sized structures, the center-to-center distances of the thin films prepared with 50, 100, 150, and 200 µL hydrochloric acid are (80 ± 9), (115 ± 9), (166 ± 40), and (190 ± 50) nm. The corresponding structure radii are (20 ± 3), (22 ± 2), (21 ± 2), and (20 ± 2) nm. The calculated pore sizes are (40 ± 14), (71 ± 13), (124 ± 44), and (150 ± 54) nm. Due to the existence of large vesicles within the thin film prepared with 200 µL hydrochloric acid, an additional large structure with center-to-center distance of (300 ± 80) nm and a radius of (22 ± 2) nm is used for modeling, which results in a calculated pore size of (256 ± 84) nm.

In order to compare with the calculated pore sizes based on the GISAXS modeling, the pore size distribution profiles are extracted through a binarization algorithm with the Image J software (Figure S4, Supporting Information) for all SEM images of Figure 3. The peak center of the profiles is determined with a Gaussian function. For the THF system, a monotonic shift of the peak center from 21 ± 3 to 25 ± 3 nm is observed, which is generally consistent with the GISAXS results (from 20 ± 4 to 30 ± 4 nm). For the 1,4-dioxane system, no distinct peak is detected for the thin film prepared with 200 µL hydrochloric acid addition, which can be attributed to the limited data points collected from the SEM images. However, it is noteworthy that more large pore sizes are detected for the thin films prepared with 150 and 200 µL hydrochloric acid, which arise from the cylindrical and vesicle structures shown in Figure 3g,h. When the hydrochloric acid addition is increased from 50 to 150 µL, the determined peak center shifts from 20 ± 3 to 36 ± 4 nm, which is in a good agreement with the GISAXS results (from 20 ± 3 to 33 ± 3 nm) as well. The good consistency of the pore sizes acquired from the GISAXS modeling and the binarization algorithm is indicative of having similar surface and inner film morphologies as probed with SEM and GISAXS, respectively.

2.4. Mechanism of Morphology Change

Considering the nonionizing properties of the PS and PEO blocks and the low dielectric constant of the solvent (THF: 7.58, 1,4-dioxane: 2.25) utilized in the present work, the repulsion force among the polymer chains provoked by ionization is negligible.[63] Accordingly, the morphology variation of the SnO₂ thin films is analyzed using the polymer–solvent interaction parameter χ[64]

$$\chi_{P-S} = V_S (\delta_S - \delta_P)^2 / RT + 0.34 \qquad (5)$$

where V_S and δ_S are the molar volume and solubility parameter of the solvent, δ_P is the solubility parameter of the polymer, R is the gas constant, and T is the temperature. As described in the Experimental Section, the SnCl₄ content added in all solutions is 33.8 µL, and the corresponding hydrochloric acid content is linearly increased from 50 to 200 µL. Thus, 20.36 mg water is required for the hydrolysis of 33.8 µL SnCl₄, whereas 50 µL of 37% hydrochloric acid solution contains 37.8 mg water already.[65] Consequently, the water content in all prepared

**ADVANCED
SCIENCE NEWS**

www.advancedsciencenews.com

**ADVANCED
MATERIALS
INTERFACES**

www.advmatinterfaces.de

Table 4. $\Delta\chi$ values calculated from different polymer–solvent interaction parameters (χ_{P-S}).

Solvent	THF				1,4-dioxane			
Hydrochloric acid content (µL)	50	100	150	200	50	100	150	200
Water content (µL)[a]	17	55	93	131	17	55	93	131
$\Delta\chi$	0.04	0.08	0.12	0.15	0.14	0.18	0.21	0.25

[a]Water content (µL) in the table refers to the water content in the hydrochloric acid except the portion consumed by SnCl₄.

sol–gel solutions is in stoichiometric excess for the hydrolysis of SnCl₄. Accordingly, the following chemical reaction equilibrium is supposed to exist in the sol–gel solution

$$SnCl_4 + xH_2O \leftrightarrow Sn(OH)_x Cl_{4-x} + xHCl (0 \le x \le 4) \quad (6)$$
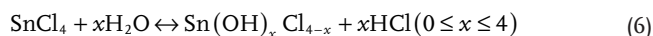
As a poor solvent for the hydrophobic PS block of the diblock copolymer PS-b-PEO, the water content in the hydrochloric acid solution significantly affects the phase separation behavior of the sol–gel solution. Furthermore, superior miscibility of water in THF or 1,4-dioxane solvent can be achieved through hydrogen-bond interaction.[66–70] Accordingly, the water content in the hydrochloric acid solution is treated as solvent except for the part consumed by the complete hydrolysis of SnCl₄.

The characteristics of different solvents and polymers can be found in the polymer handbook (Table S2, Supporting Information).[71] As shown in Equation (7), the solubility parameter of the solvent (Hansen solubility parameter δ_H) consists of three parts: dispersive δ_d, permanent dipole–dipole interaction δ_p, and hydrogen bonding forces δ_h

$$\delta_H^2 = \delta_d^2 + \delta_p^2 + \delta_h^2 \quad (7)$$

The solubility parameter ($\delta_{H,\ mixture}$) and the molar volume ($V_{S,\ mixture}$) of the binary mixture of THF/H₂O or 1,4-dioxane/H₂O are taken as the sum of the products of the component value with their volume fractions

$$\delta_{H,mixture} = \sum \delta_i \varphi_i; \ V_{S,mixture} = \sum V_i \varphi_i \quad (8)$$

δ_i, V_i, and φ_i refer to the solubility parameter, molar volume, and the volume fraction of each single component in the solvent mixture, respectively. The calculated solubility parameter ($\delta_{H,\ mixture}$) and the molar volume ($V_{S,\ mixture}$) of different binary mixtures are listed in Table S3 in the Supporting Information.

Based on the existing literature and calculated parameters (in Tables S2 and S3, Supporting Information), the polymer–solvent interaction parameters (χ_{P-S}) of different polymer–solvent pairs are determined (Table S4, Supporting Information).

The preferential affinity of a solvent for a certain block is represented by an expression of $\Delta\chi = \chi_{PS-S} - \chi_{PEO-S}$. **Table 4** lists the calculated $\Delta\chi$ values from the different polymer–solvent interaction parameters (χ_{P-S}). According to the Flory–Huggins theory, the polymer can be completely dissolved in the solvent over the entire composition range when the $\Delta\chi$ value is lower than 0.5.[72] As shown in Table 4, the calculated $\Delta\chi$ values for all solvent mixtures utilized in the present work are less than 0.5, which suggests that both PS blocks and PEO blocks of the

PS-b-PEO template can be well dissolved in the solvent. Since the water comprised in the hydrochloric acid is a significant factor affecting the preferential affinity of the solvent to the different polymer blocks, the morphology variation of the SnO₂ thin films is discussed in detail with respect to the water content in the sol–gel solution. **Figure 5** shows the different film morphologies determined by the water content and $\Delta\chi$ values. It is observed that the $\Delta\chi$ values for both, THF and 1,4-dioxane mixture, monotonously increase with the increase of the water content. A spherical pore structure is preferentially formed for lower $\Delta\chi$ values ($0.04 \le \Delta\chi \le 0.18$). When the $\Delta\chi$ value reaches 0.21, a hybrid morphology consisting of spherical and cylindrical porous structures is observed. Further increasing the $\Delta\chi$ value to 0.25 leads to the appearance of vesicle structures. The structure transition from sphere to vesicle in terms of the $\Delta\chi$ values can be explained by the different stretching of the PS blocks in the sol–gel solution. The introduced water increases the surface energy between the PS chains and the surrounding solvent, which significantly inhibits the PS chain stretching in the solution. The PS chains in spherical micelles are typically more stretched than in cylinders or vesicles. Accordingly, they are usually the first aggregates to form and can be considered as the starting morphology for other aggregates.[62–65] It should be noted that the calculated $\Delta\chi$ value for the SnO₂ thin film prepared with 50 µL hydrochloric acid (corresponding to 17 µL
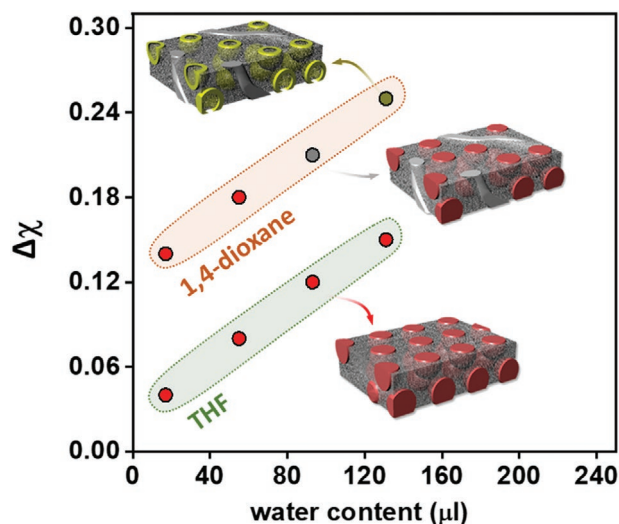

Figure 5. Microstructure distribution of the SnO₂ thin films prepared with different solvent (THF or 1,4-dioxane) and water content (from hydrochloric acid), resulting in different film morphologies described as spheres (red), hybrid morphology of spheres and cylinders (gray), and vesicles (yellow).

water) and 1,4-dioxane solvent is located in the $\Delta\chi$ value range obtained with THF system ($0.04 \leq \Delta\chi \leq 0.15$). However, compared to the random porous structures shown in Figure 3a–d, a significantly enhanced order of the pore arrangement is observed in Figure 3e. This difference in order can be tentatively explained by a different hydrogen bond interaction type between the employed cycloether (THF or 1,4-dioxane) and H_2O. For a cycloether/H_2O binary mixture, the interactions between cycloether molecules can be mediated by H_2O molecules through bifunctional donor and acceptor hydrogen bond interactions.[66,72] In contrast to the 1,4-dioxane/H_2O mixture, the smaller size of the THF molecule has an unfavorable effect on the hydrogen bond network formed between H_2O molecules. This leads to a significantly enhanced micro-heterogeneity in the THF/H_2O mixture system. As a result, THF/H_2O clusters enriched in THF are formed.[73] The formation of THF/H_2O clusters circumvents the unfavorable interactions between water and the hydrophobic PS chains of the block copolymer, which weakens the phase separation tendency of the block copolymer. Accordingly, compared to the hexagonally packed pore arrangement obtained with 1,4-dioxane (Figure 3e), a reduction in number and order of the pore structures is observed in the THF system (Figure 3a–d).

3. Conclusion

In this work, the amphiphilic block copolymer-templated SnO_2 thin film synthesis is systematically investigated in terms of the solvent category and hydrochloric acid content. Two kinds of cycloether solvents, THF and 1,4-dioxane, are utilized as good solvent for dissolution of the block copolymer PS-*b*-PEO. Hydrochloric acid is added as a poor solvent for stimulating the phase separation of the block polymer and to be the catalyst for the hydrolysis of $SnCl_4$. SEM and GISAXS measurements are performed to detect the mesoscale structure of the thin films at different length scales. A detailed comparison and analysis demonstrates that the structural transformation of the SnO_2 thin films in terms of different solvent category and hydrochloric acid addition is governed by a synergistic effect of the following two factors: First, the preferential affinity of the solvent for a certain block; second, the hydrogen bond interaction between the employed cycloether and H_2O. By tuning the preferential affinity of the mixed solvent with different hydrochloric acid content, various structures including spheres, cylinders, and vesicles are obtained. Specifically, the spherical pore structure is preferentially formed at relative low $\Delta\chi$ value ($0.04 \leq \Delta\chi \leq 0.18$). A hybrid morphology consists of spherical and cylindrical porous structures can be obtained when the $\Delta\chi$ value reaches a value of 0.21. Further increasing the $\Delta\chi$ value to 0.25 provokes the formation of vesicle structures. Compared to 1,4-dioxane, the smaller molecule size of THF leads to the enhanced micro-heterogeneity in the THF/H_2O mixture. Consequently, all the thin films prepared with THF solvent show random mesoporous structures. Irrespective of the morphology, all the prepared SnO_2 thin films consist cassiterite phase crystals with small sizes, which can be foreseen to have tremendous application potential in gas sensors, photocatalysis, and photovoltaics.

4. Experimental Section

Materials: Polystyrene-block-polyethylene oxide (PS$_{20500}$-*b*-PEO$_{8000}$) was obtained from Polymer Source Inc. Tin chloride ($SnCl_4$, 98%), THF (99.9%), 1,4-dioxane (99.8%), and concentrated hydrochloric acid (37%) were purchased from Sigma-Aldrich and used without further purification.

Sol–Gel Stock Solution Preparation: For investigating the effect of the solvent category and poor solvent addition on the thin film morphology, two different solvents (THF and 1,4-dioxane) and four different hydrochloric acid volumes (50, 100, 150, and 200 µL) were utilized for the sol–gel stock solution preparation. In order to prevent the formation of big clusters due to the vigorous hydrolysis reaction of the $SnCl_4$ precursor, 2.0 mL THF or 1,4-dioxane solvent were divided into smaller portions of 1.5 and 0.5 mL for the stock solution preparation. 1.5 mL THF or 1,4-dioxane was utilized for dispersing PS-*b*-PEO and $SnCl_4$ precursor, the rest 0.5 mL THF or 1,4-dioxane was assigned for diluting different volumes of hydrochloric acid (50, 100, 150, and 200 µL). First, 21.0 mg PS-*b*-PEO was added into 1.5 mL THF or 1,4-dioxane solvent followed by 1 h continuous stirring to fully dissolve it. Then, 33.8 µL $SnCl_4$ and 0.5 mL diluted hydrochloric acid solution were sequentially pipetted into the well-dissolved PS-*b*-PEO solution. Because of the complexation effect between THF or 1,4-dioxane solvent and $SnCl_4$ molecules, white crystalline solids were formed once adding $SnCl_4$ to the solution (Figure 1a and Figure S1, Supporting information). However, the complex crystals were moisture sensitive and rapidly vanished with the addition of diluted hydrochloric acid solution.[49,56] The corresponding component phase diagram of the samples prepared with THF or 1,4-dioxane solvent is shown in **Figure 6**. The as-prepared sol–gel solution was further stirred for 1 h to stabilize the hydrogen bonds formed between the hydrophilic PEO blocks and the hydrolyzed $(HO)_X SnCl_{4-X}$ species.

Thin Film Preparation: For the thin film deposition, the as-prepared sol–gel solutions were spin coated on pre-cleaned silicon substrates with a Delta 6 RC TT spin coater (SÜSS Micro Tec Lithography GmbH) at 2000 rpm for 60 s. For removing the polymer template, the as-spun thin films were calcined at 500 °C for 2 h with a heating rate of 1 °C min^{-1} in ambient atmosphere.

Thin Film Characterization: The surface morphology of the prepared SnO_2 thin films was probed with a high-resolution field-emission SEM (Zeiss Gemini NVision 40) at a working distance of 3.5 mm and an acceleration voltage of 5 kV. For the cross-section SEM measurement, the thin films were tilted at 45° respective to the electron beam for a
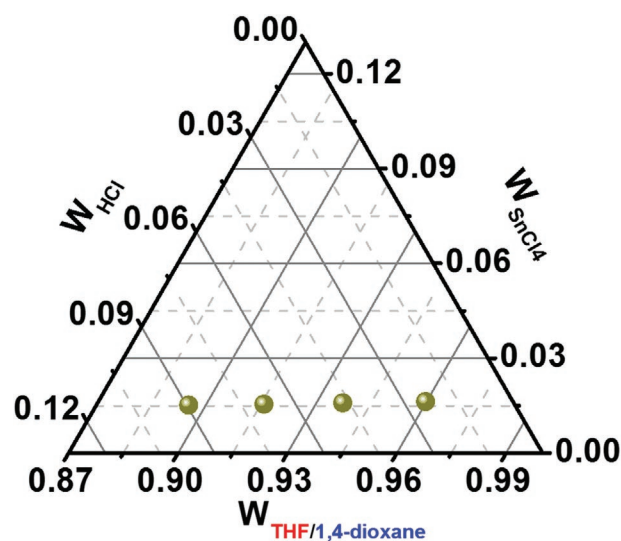

Figure 6. Component phase diagram of the samples prepared with THF or 1,4-dioxane solvent. $W_{component}$ refers to the volume fraction of the component.

**ADVANCED
SCIENCE NEWS**

www.advancedsciencenews.com

**ADVANCED
MATERIALS
INTERFACES**

www.advmatinterfaces.de

better view. The statistical average information of the porous structures within the bulk films was detected with GISAXS at the P03 beamline of PETRA III storage ring.[57] The measurements were performed with a wavelength of 0.96 Å and at an incidence angle of 0.4°. A sample to detector distance of 4200 mm was utilized to obtain an appropriate q range. The scattering signal was recorded by a Pilatus 300K (Dectris Ltd.) detector with a pixel size of 172 μm. A python program named Directly Programmable Data Analysis Kit (DPDAK) was used for calibration and data analysis.[58] Horizontal line cuts of the 2D GISAXS data were performed at the Yoneda peak position of the SnO_2. The crystallinity of the prepared SnO_2 thin films was investigated with a D8 ADVANCE X-ray diffractometer using an X-ray wavelength of 1.54 Å.

Supporting Information

Supporting Information is available from the Wiley Online Library or from the author.

Acknowledgements

Conflict of interest

The authors declare no conflict of interest.

Keywords

[1] H. X. Deng, S. S. Li, J. Li, *J. Phys. Chem. C* **2010**, *114*, 4841.
[2] Y. Q. Luo, Y. Tang, S. Zheng, Y. Yan, H. G. Xue, H. Pang, *J. Mater. Chem. A* **2018**, *6*, 4236.
[3] D. Pan, N. Wan, Y. Ren, W. Zhang, X. Lu, Y. Wang, Y. S. Hu, Y. Bai, *ACS Appl. Mater. Interfaces* **2017**, *9*, 9747.
[4] T. Ma, X. Yu, H. Li, W. Zhang, X. Cheng, W. Zhu, X. Qiu, *Nano Lett.* **2017**, *17*, 3959.
[5] M. S. Faramarzi, A. Abnavi, S. Ghasemi, Z. Sanaee, *Mater. Res. Express* **2018**, *5*, 065040.
[6] F. Zoller, K. Peters, P. M. Zehetmaier, P. Zeller, M. Döblinger, T. Bein, Z. K. Sofer, D. Fattakhova-Rohlfing, *Adv. Funct. Mater.* **2018**, *28*, 1706529.
[7] Y. Lee, M. R. Jo, K. Song, K. M. Nam, J. T. Park, Y. M. Kang, *ACS Appl. Mater. Interfaces* **2012**, *4*, 3459.
[8] Z. W. Zhou, Y. T. Liu, X. M. Xie, X. Y. Ye, *ACS Appl. Mater. Interfaces* **2016**, *8*, 7092.
[9] W. Dong, J. Xu, C. Wang, Y. Lu, X. Liu, X. Wang, X. Yuan, Z. Wang, T. Lin, M. Sui, I. W. Chen, F. Huang, *Adv. Mater.* **2017**, *29*, 1700136.
[10] G. Du, Z. Guo, P. Zhang, Y. Li, M. Chen, D. Wexler, H. Liu, *J. Mater. Chem.* **2010**, *20*, 5689.
[11] Y. E. Roginskaya, F. K. Chibirova, T. L. Kulova, A. M. Skundin, *Russ. J. Electrochem.* **2006**, *42*, 355.
[12] B. Roose, C. M. Johansen, K. Dupraz, T. Jaouen, P. Aebi, U. Steiner, A. Abate, *J. Mater. Chem. A* **2018**, *6*, 1850.
[13] Y. Rui, H. Xiong, B. Su, H. Wang, Q. Zhang, J. Xu, P. Müller-Buschbaum, *Electrochim. Acta* **2017**, *227*, 49.
[14] N. Li, J. Yan, Y. Ai, E. Jiang, L. Lin, C. Shou, B. Yan, J. Sheng, J. Ye, *Sci. China Mater.* **2020**, *63*, 207.
[15] B. Roose, J. P. C. Baena, K. C. Gödel, M. Graetzel, A. Hagfeldt, U. Steiner, A. Abate, *Nano Energy* **2016**, *30*, 517.
[16] A. Fakharuddin, F. Di Giacomo, I. Ahmed, Q. Wali, T. M. Brown, R. Jose, *J. Power Sources* **2015**, *283*, 61.
[17] Q. Jiang, X. Zhang, J. You, *Small* **2018**, *14*, 1801154.
[18] X. Zhang, Y. Rui, Y. Wang, J. Xu, H. Wang, Q. Zhang, P. Müller-Buschbaum, *J. Power Sources* **2018**, *402*, 460.
[19] Y. Chen, Q. Meng, L. Zhang, C. Han, H. Gao, Y. Zhang, H. Yan, *J. Energy Chem.* **2019**, *35*, 144.
[20] D. Mohanta, M. Ahmaruzzaman, *RSC Adv.* **2016**, *6*, 110996.
[21] Y. Gun, G. Y. Song, V. H. Quy, J. Heo, H. Lee, K. S. Ahn, S. H. Kang, *ACS Appl. Mater. Interfaces* **2015**, *7*, 20292.
[22] E. Brunet, T. Maier, G. C. Mutinati, S. Steinhauer, A. Köck, C. Gspan, W. Grogger, *Sens. Actuators, B* **2012**, *165*, 110.
[23] T. Tharsika, M. Thanihaichelvan, A. S. M. A. Haseeb, S. A. Akbar, *Front. Mater.* **2019**, *6*, 80.
[24] I. H. Kadhim, H. A. Hassan, Q. N. Abdullah, *Nano-Micro Lett.* **2016**, *8*, 20.
[25] X. Xiao, L. Liu, J. Ma, Y. Ren, X. Cheng, Y. Zhu, D. Zhao, A. A. Elzatahry, A. Alghamdi, Y. Deng, *ACS Appl. Mater. Interfaces* **2018**, *10*, 1871.
[26] M. M. H. Bhuiyan, T. Ueda, T. Ikegami, *Solid State Phenom.* **2007**, *124–126*, 223.
[27] T. Oyabu, *J. Appl. Phys.* **1982**, *53*, 2785.
[28] M. Di Giulio, G. Micocci, A. Serra, A. Tepore, R. Rella, P. Siciliano, *Sens. Actuators, B* **1995**, *25*, 465.
[29] K. Haddad, A. Abokifa, S. Kavadiya, B. Lee, S. Banerjee, B. Raman, P. Banerjee, C. Lo, J. Fortner, P. Biswas, *ACS Appl. Mater. Interfaces* **2018**, *10*, 29972.
[30] W. S. Chi, C. S. Lee, H. Long, M. H. Oh, A. Zettl, C. Carraro, J. H. Kim, R. Maboudian, *ACS Appl. Mater. Interfaces* **2017**, *9*, 37246.
[31] S. Park, S. An, Y. Mun, C. Lee, *ACS Appl. Mater. Interfaces* **2013**, *5*, 4285.
[32] T. Zhao, P. Qiu, Y. Fan, J. Yang, W. Jiang, L. Wang, Y. Deng, W. Luo, *Adv. Sci.* **2019**, *6*, 1902008.
[33] J. Jeong, S. P. Choi, C. I. Chang, D. C. Shin, J. S. Park, B. T. Lee, Y. J. Park, H. J. Song, *Solid State Commun.* **2003**, *127*, 595.
[34] M. A. M. Akhir, K. Mohamed, H. L. Lee, S. A. Rezan, *Procedia Chem.* **2016**, *19*, 993.
[35] X. Zhou, L. J. Wan, Y. G. Guo, *Adv. Mater.* **2013**, *25*, 2152.
[36] K. C. Song, J. H. Kim, *J. Colloid Interface Sci.* **1999**, *212*, 193.
[37] G. Zhang, M. Liu, *J. Mater. Sci.* **1999**, *34*, 3213.
[38] S. Mohana Priya, A. Geetha, K. Ramamurthi, *J. Sol-Gel Sci. Technol.* **2016**, *78*, 365.
[39] M. Aziz, S. S. Abbas, W. R. W. Baharom, W. Z. W. Mahmud, *Mater. Lett.* **2012**, *74*, 62.
[40] M. Aziz, S. Saber Abbas, W. R. Wan Baharom, *Mater. Lett.* **2013**, *91*, 31.
[41] W. Luo, J. Deng, Q. Fu, D. Zhou, Y. Hu, S. Gong, Z. Zheng, *Sens. Actuators, B* **2015**, *217*, 119.

**ADVANCED
SCIENCE NEWS**

www.advancedsciencenews.com

**ADVANCED
MATERIALS
INTERFACES**

www.advmatinterfaces.de

[42] R. Dujardin, F. Delorme, B. Pintault, P. Belleville, C. Autret, I. Monot-Laffez, F. Giovannelli, *Mater. Lett.* **2017**, *187*, 151.

[43] J. Zhang, L. Gao, *J. Solid State Chem.* **2004**, *177*, 1425.

[44] S. Zhang, P. Zhang, Y. Wang, Y. Ma, J. Zhong, X. Sun, *ACS Appl. Mater. Interfaces* **2014**, *6*, 14975.

[45] Y. Liu, E. Koep, M. Liu, *Chem. Mater.* **2005**, *17*, 3997.

[46] A. Katoch, J. H. Kim, Y. J. Kwon, H. W. Kim, S. S. Kim, *ACS Appl. Mater. Interfaces* **2015**, *7*, 11351.

[47] M. Dirican, Y. Lu, Y. Ge, O. Yildiz, X. Zhang, *ACS Appl. Mater. Interfaces* **2015**, *7*, 18387.

[48] W. Luo, T. Zhao, Y. Li, J. Wei, P. Xu, X. Li, Y. Wang, *J. Am. Chem. Soc.* **2016**, *138*, 12586.

[49] T. Brezesinski, A. Fischer, K. I. Iimura, C. Sanchez, D. Grosso, M. Antonietti, B. M. Smarsly, *Adv. Funct. Mater.* **2006**, *16*, 1433.

[50] Y. J. Cheng, J. S. Gutmann, *J. Am. Chem. Soc.* **2006**, *128*, 4658.

[51] Y. J. Cheng, S. Zhou, M. Wolkenhauer, G. G. Bumbu, S. Lenz, M. Memesa, S. Nett, S. Emmerling, W. Steffen, S. V. Roth, J. S. Gutmann, *Eur. J. Inorg. Chem.* **2014**, *2014*, 836.

[52] N. Hohn, S. J. Schlosser, L. Bießmann, L. Song, S. Grott, S. Xia, K. Wang, M. Schwartzkopf, S. V. Roth, P. Müller-Buschbaum, *ACS Appl. Nano Mater.* **2018**, *1*, 4227.

[53] Y. J. Cheng, S. Zhou, J. S. Gutmann, *Macromol. Rapid Commun.* **2007**, *28*, 1392.

[54] C. Sanchez, C. Boissiere, D. Grosso, C. Laberty, L. Nicole, *Chem. Mater.* **2008**, *20*, 682.

[55] Y. J. Cheng, M. Wolkenhauer, G. G. Bumbu, J. S. Gutmann, *Macromol. Rapid Commun.* **2012**, *33*, 218.

[56] M. Bauer1, J. Kouvetakis, L. Groy, Z. *Kristallogr. - New Cryst. Struct.* **2002**, *217*, 421.

[57] A. Buffet, A. Rothkirch, R. Döhrmann, V. Körstgens, M. M. Abul Kashem, J. Perlich, G. Herzog, M. Schwartzkopf, R. Gehrke, P. Müller-Buschbaum, S. V. Roth, *J. Synchrotron Radiat.* **2012**, *19*, 647.

[58] G. Benecke, W. Wagermaier, C. Li, M. Schwartzkopf, G. Flucke, R. Hoerth, I. Zizak, M. Burghammer, E. Metwalli, P. Müller-Buschbaum, M. Trebbin, *J. Appl. Crystallogr.* **2014**, *47*, 1797.

[59] H. M. Hdz-Garcia, A. I. Martinez, in *Proc. 4th WSEAS Int. Conf. Circuits, Systems, Signal and Telecommunications* (Eds: S. Lagakos, L. I. Perlovsky), Harward University, Cambridge **2010**, pp. 144–146.

[60] J. J. van Franeker, D. Hermida-Merino, C. Gommes, K. Arapov, J. J. Michels, R. A. J. Janssen, G. Portale, *Adv. Funct. Mater.* **2017**, *27*, 1702516.

[61] K. Wang, V. Körstgens, D. Yang, N. Hohn, S. V. Roth, P. Müller-Buschbaum, *J. Mater. Chem. A* **2018**, *6*, 4405.

[62] K. Sarkar, C. J. Schaffer, D. M. González, A. Naumann, J. Perlich, P. Müller-Buschbaum, *J. Mater. Chem. A* **2014**, *2*, 6945.

[63] Y. Mai, A. Eisenberg, *Chem. Soc. Rev.* **2012**, *41*, 5969.

[64] L. He, S. Pan, J. Peng, *J. Polym. J. Polym. Sci., Part B: Polym. Phys.* **2016**, *54*, 544.

[65] N. S. Cameron, M. K. Corbierre, A. Eisenberg, *Can. J. Chem.* **1999**, *77*, 1311.

[66] A. C. Kumbharkhane, Y. S. Joshi, S. C. Mehrotra, S. Yagihara, S. Sudo, *Phys. B* **2013**, *421*, 1.

[67] D. Sharma, S. Sahoo, B. K. Mishra, *J. Mol. Model.* **2014**, *20*, 2408.

[68] A. Chaudhari, *Int. J. Quantum Chem.* **2010**, *110*, 1092.

[69] M. J. Shultz, T. H. Vu, *J. Phys. Chem. B* **2015**, *119*, 9167.

[70] K. Mizuno, S. Imafuji, T. Fujiwara, T. Ohta, Y. Tamiya, *J. Phys. Chem. B* **2003**, *107*, 3972.

[71] A. F. M. Barton, *Handbook of Solubility Parameters and Other Cohesive Parameters*, CRC Publishers, Boca Raton, FL **1983**.

[72] Y. Li, H. Huang, T. He, Y. Gong, *J. Phys. Chem. B* **2010**, *114*, 1264.

[73] T. Takamuku, A. Nakamizo, M. Tabata, K. Yoshida, T. Yamaguchi, T. Otomo, *J. Mol. Liq.* **2003**, *103–104*, 143.